Effects of alkyl chain length and anion size on thermal and structural properties for 1-alkyl-3-methylimidazolium hexafluorocomplex salts (C(x)MImAF6, x = 14, 16 and 18; A = P, As, Sb, Nb and Ta).

AUTHOR(S):

Xu, Fei; Matsumoto, Kazuhiko; Hagiwara, Rika

CITATION:

Xu, Fei ...[et al]. Effects of alkyl chain length and anion size on thermal and structural properties for 1-alkyl-3-methylimidazolium hexafluorocomplex salts (C(x)MImAF6, x = 14, 16 and 18; A = P, As, Sb, Nb and Ta).. Dalton transactions 2012, 41: 3494-3502

ISSUE DATE:

2012-01-31

URL:

http://hdl.handle.net/2433/169693

Effects of Alkyl Chain Length and Anion Size on Thermal and Structural Properties for 1-Alkyl-3-methylimidazolium Hexafluorocomplex Salts (C_xMImAF_6, x = 14, 16, and 18; A = P, As, Sb, Nb, and Ta)

Fei Xu, Kazuhiko Matsumoto*, Rika Hagiwara

Graduate School of Energy Science, Kyoto University, Yoshida, Sakyo-ku, Kyoto 606-8501, Japan

*Email: k-matsumoto@energy.kyoto-u.ac.jp

Abstract

A series of 1-alkyl-3-methylimidazolium hexafluorocomplex salts (C_xMImAF_6, *x* = 14, 16, and 18, A = P, As, Sb, Nb, and Ta) have been characterized by thermal analysis, X-ray diffraction, and polarized optical microscopy. Liquid crystalline mesophase is observed for all the C_{16}MIm and C_{18}MIm salts. The $C_{14}MIm^+$ cation gives a liquid crystalline mesophase only with PF_6^-. Temperature range of the liquid crystalline mesophase increases with increase in alkyl chain length or with decrease in anion size. Single-crystal X-ray diffraction revealed that all the C_{18}MImAF_6 salts (A = P, As, Sb, Nb, and Ta) are isostructural with each other in the crystalline phase and have a layered structure. Interdigitated alkyl chain of the cation has a bent shape like a spoon near the imidazolium ring in the crystalline phase at –100 °C and is tilted to the sheets of the imidazolium headgroups and anions. Increase of temperature increases the ratio of an all-trans conformation to the bent conformation in the crystalline phase. X-ray diffraction and polarized optical microscopy suggested that the liquid crystalline mesophase has a smectic A_2 structure. The interlayer distance increases with decrease in the anion size since the smaller anion has a stronger coulombic interaction to the imidazolium headgroup, resulting in the decrease of interdigitated part to give a larger layer spacing.

Keywords: ionic liquids crystals, mesophase, imidazolium, hexafluorocomplex

Electronic supplementary information (ESI) available: Infra-red spectra, Raman spectra, thermogravimetric curves, additional differential scanning calorimetric curves, additional polarized optical microscopic textures, additional X-ray diffraction patterns,

additional layer spacings, crystallographic data in CIF format, and additional geometrical parameters. See DOI: xx.xxxx/xxxx. CCDC reference numbers 843137-843151

Introduction

Ionic liquid crystals (ILCs) are composed of only ionic species and have anisotropic structural organizations,[1] which make them attractive as one-dimensional[2-4] or two-dimensional[5-7] ion-conduction materials to move a specific ion as well as anisotropic reaction media. Ionic liquids are attracting more and more attention as functional materials because of their unique characteristics such as wide liquid temperature range, negligible vapor pressure, and nonflammability.[8] Because of the widespread use of imidazolium-based ionic liquids with low melting point and low viscosity, imidazolium-based ILCs are frequently studied.[9] Thermal behavior of ILCs based on imidazolium cations with functional groups depends on the number of mesogenic units, mesogenic promoter, and counteranion.[10] Although a variety of functional groups such as a cholesterol group were coupled with the imidazolium cation to form liquid crystalline mesophase,[10] ILCs based on imidazolium cation with a simple alkyl chain are common in previous reports to examine the effects of alkyl chain and anion on physical properties. A series of 1-alkyl-3-methylimidazolium cations (C_xMIm^+) with long alkyl chains were combined with various anions such as chloride (Cl^-),[11] bromide (Br^-),[12] tetrachlorometallate (MCl_4^-, M = Co and Ni),[11] trifluoromethylsulfonate ($OSO_2CF_3^-$),[12] tetrafluoroborate (BF_4^-),[13] and hexafluorophosphate (PF_6^-).[14] The temperature range of mesophase observed for these salts increases with increasing alkyl chain length, although the alkyl chain length where liquid crystalline mesophase appears depends on the anionic species.

Although the C_xMImPF_6-type ILCs were studied by differential scanning calorimetry (DSC), polarized optical microscopy (POM), X-ray diffraction (XRD), other C_xMImAF_6 (AF_6^- = hexafluorocomplex anion) ILCs were not. Liquid crystalline mesophase appears with x = 14 in the case of C_xMImPF_6, and the temperature range

of mesophase rapidly increases with increase in *x*. The cations of $C_{12}MImPF_6$ and $C_{14}MImPF_6$ in the crystalline phase show a "spoon-like" shape with the alkyl chains interdigitated to form nonpolar layers, separating the polar layers made up of imidazolium headgroups and anions.[14-16] In this study, a series of C_xMImAF_6 salts (*x* = 14, 16, and 18, A = P, As, Sb, Nb, and Ta) were synthesized and characterized by DSC, POM, and XRD to systematically investigate effects of the alkyl chain length and anion size on their thermal and structural properties.

Results and discussion

Thermal Properties

All the obtained salts are white hydrophobic solid at room temperature and only $C_xMImNbF_6$ is gradually hydrolyzed in the air even at room temperature. The AF_6^- anion is best identified by IR and Raman spectroscopy (Experimental Section and Figure S1-S6).[17] Table 1 summarizes the DSC data (phase transition temperature, ΔH, and ΔS) for all the C_xMImAF_6 salts. Figure 1 shows the DSC curves of $C_{18}MImAF_6$. Two endothermic peaks are observed in all the cases. The peaks at the lower and higher temperatures correspond to melting point (from crystal to liquid crystal) and clearing point (from liquid crystal to isotropic liquid), respectively. The relatively large ΔH (and thus ΔS) on melting indicates a large structural change, namely, the breakup of a three-dimensionally ordered crystal lattice. The small ΔH (and thus ΔS) on clearing is mainly caused by the breakup of van der Waals interactions between the alkyl chains, which is reflected in the increase of ΔH (and thus ΔS) for clearing with the increase in *x* for the same anion. Similar phenomena are also observed for ILCs of C_xMImCl, C_xMImBr, C_xMImBF_4, and $C_xMIm(FH)_2F$.[12-14,18] Either a small peak ($C_{18}MImPF_6$) or a broad peak ($C_{18}MImAF_6$, A = As, Sb, Nb, and Ta) is observed in

the crystalline phase below melting point, which is probably ascribed to conformational change of the alkyl chains (see the section of crystal structures below). An endothermic peak corresponding to clearing point is also observed in the thermograms of $C_{16}MImAF_6$ (Figure S11, Supporting Information), proving all the $C_{16}MImAF_6$ salts give liquid crystalline mesophases, although the temperature range of liquid crystal is quite narrow (~10 °C) for $C_{16}MImSbF_6$, $C_{16}MImNbF_6$, and $C_{16}MImTaF_6$. Clearing point was not observed for $C_{14}MImAF_6$ (Figure S10, Supporting Information) in the heating process at the scan rate of 5 °C min^{-1}. It is noteworthy that a small exothermic peak was observed for $C_{14}MImPF_6$ at 69.7 °C during the cooling process (Figure 2). This transition temperature is nearly the same as that for melting in the heating process and they seem to overlap. The lower scan rate of 0.5 °C min^{-1} confirmed the liquid crystalline mesophase (Figure 2, inset) although the transition temperature was slightly lower than those reported in the previous work.[14] The other four $C_{14}MImAF_6$ (A = As, Sb, Nb, and Ta) salts did not exhibit liquid crystalline mesophase even during the cooling process.

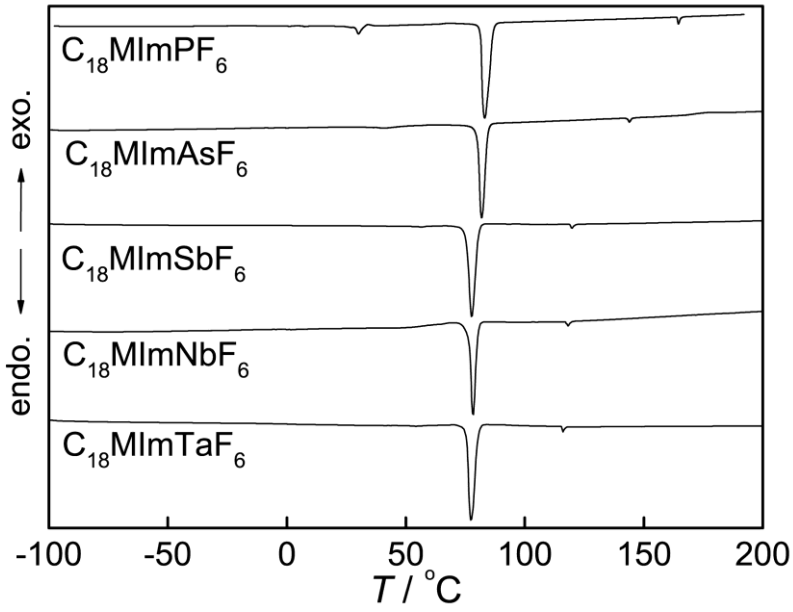

Figure 1 Differential scanning calorimetric curves (heating process) for $C_{18}MImAF_6$ (A = P, As, Sb, Nb, and Ta).

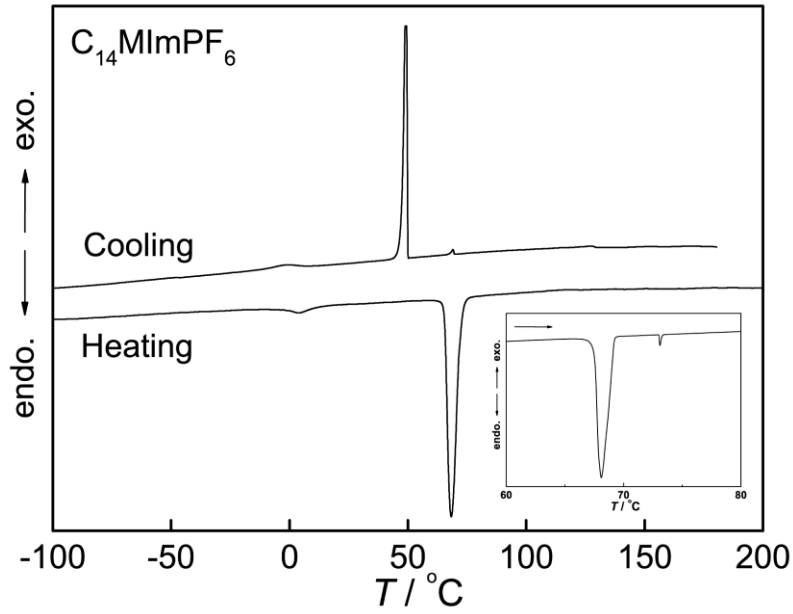

Figure 2 Differential scanning calorimetric curves of heating and cooling processes for $C_{14}MImPF_6$ at 5 °C min^{-1} and heating process at 0.5 °C min^{-1} (inset).

Table 1 Summary of DSC for C_xMImAF_6 (x = 14, 16, and 18, A = P, As, Sb, Nb, and Ta).

x	A	Transition[a]	Temperature (°C)	ΔH (kJ mol^{-1})	ΔS (J mol^{-1} K^{-1})
14	P	cryst–iso	65.1	33.1	97.8
		cryst–SmA_2[b]	67.4	36.5	107.3
		SmA_2–iso[b]	73.0	0.4	1.3
	As	cryst–iso	64.8	34.0	100.7
	Sb	cryst–iso	56.8	32.4	98.2
	Nb	cryst–iso	56.0	31.4	95.6
	Ta	cryst–iso	56.0	28.0	85.2
16	P	cryst–SmA_2	75.2	30.1	86.4
		SmA_2–iso	124.8	0.5	1.3
	As	cryst–SmA_2	74.8	36.5	105.0
		SmA_2–iso	104.3	0.6	1.5
	Sb	cryst–SmA_2	67.5	33.1	97.3
		SmA_2–iso	77.0	0.4	1.2
	Nb	cryst–SmA_2	66.9	33.0	97.2
		SmA_2–iso	77.0	0.5	1.3
	Ta	cryst–SmA_2	66.3	33.0	97.3
		SmA_2–iso	75.5	0.4	1.2
18	P	cryst–SmA_2	79.9	47.5	134.6
		SmA_2–iso	164.0	1.1	2.6
	As	cryst–SmA_2	78.1	46.3	131.9
		SmA_2–iso	142.8	0.9	2.2
	Sb	cryst–SmA_2	74.5	36.8	106.0
		SmA_2–iso	117.9	0.7	1.7
	Nb	cryst–SmA_2	74.2	31.3	90.1
		SmA_2–iso	116.9	0.7	1.9
	Ta	cryst–SmA_2	74.0	36.7	105.8
		SmA_2–iso	115.4	0.7	1.8

[a]The scan rate of 5 °C min^{-1} was used. The symbols, cryst, iso, and SmA_2 denote crytstal, isotropic liquid, and smectic A_2 liquid crystal, respectively. [b]These transitions were determined from DSC recorded at 0.5 °C min^{-1}.

Figure 3 shows the melting and clearing points of C_xMImAF_6 as a function of the carbon number x and the radius of the central atom of AF_6^-.[19] Both the melting and clearing points increase with the increase in x or the decrease in the size of anion. The larger temperature dependence of clearing point than that of melting point results in the increase in temperature range of liquid crystalline mesophase with increase in x or decrease in the size of anion. The increase of melting point against x can be explained by increase of the van der Waals interactions between the alkyl chains, which leads to clearer separation of polar (imidazolium headgroup and anion) and nonpolar (long alkyl chain) regions.[13] When the size of AF_6^- is changed with the fixed cationic structure, the difference in temperature dependence of melting and clearing points

reflects the strength of the interaction between the imidazolium headgroup and the anion. These trends suggest both the van der Waals interaction between the alkyl chains and the electrostatic interaction between the cation and anion have an effect to stabilize the liquid crystalline mesophase, and this also explains the phenomena that the alkyl chain length where liquid crystalline mesophases are observed depends on the anionic species in the cases of C_xMIm salts.[11-14,18] Compared with symmetric *N*,*N*'-dialkylimidazolium salts with long alkyl chains, C_xMIm salts show different thermal behavior probably due to the weaker van der Waals interactions based on the different number of long alkyl chains.[20-22] For PF_6^- salts, both the melting and clearing points decrease by introducing another long alkyl chain (melting and clearing points of C_{16}MImPF_6 are 75.2 and 124.8 °C and melting and clearing points of $C_{16}C_{16}$ImPF_6 are 61.3 and 103.3 °C).[22] Another example, $PdCl_4^{2-}$ salts, gives a different trend; melting and clearing points decrease and increase, respectively, by introducing another long alkyl chain (melting and clearing points of (C_{16}MIm)($PdCl_4$) are 124 and 190 °C and melting and clearing points of $(C_{16}C_{16})_2PdCl_4$ are 94.9 and 214.6 °C). The difference in charges of the anions may cause this behavior.

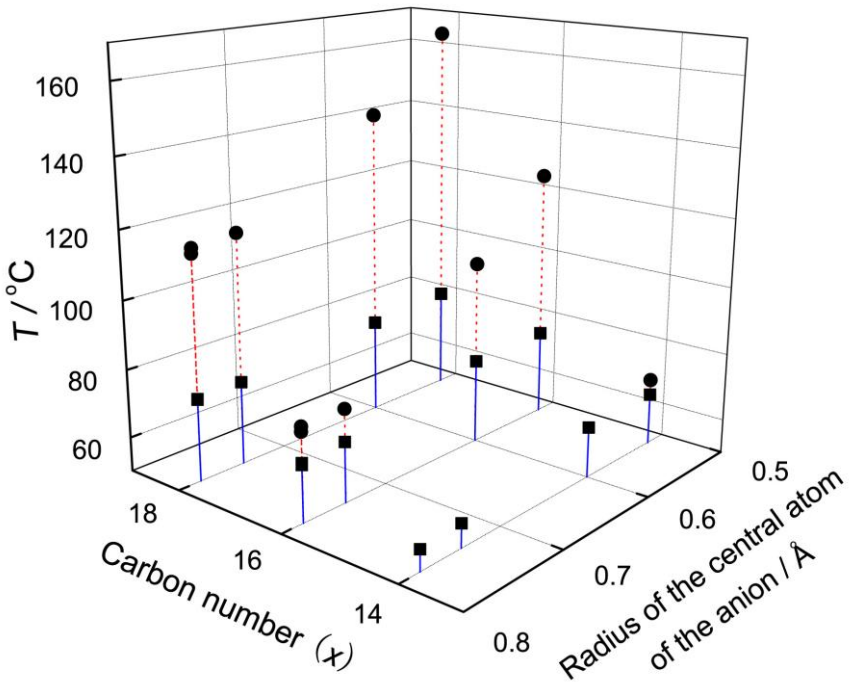

Figure 3 Melting points (■) and clearing points (●) observed in the DSC thermogram of C_xMImAF_6 (x = 14, 16, and 18, A = P, As, Sb, Nb, and Ta).

Structural properties

The five kinds of $C_{18}MImAF_6$ salts are isostructural with each other since the cation with a long alkyl chain dominates crystal packing, although a slight increase in cell volume is observed with increasing anion size. This is in contrast with the cases of a series of EMIm salts, where the PF_6, AsF_6, and SbF_6 salts belong to a monoclinic cell (space group: $P2_1/c$) and the NbF_6 and TaF_6 salts belong to an orthorhombic cell (space group: $P2_12_12_1$).[23] The crystal structure of $C_{18}MImTaF_6$ at –100 °C, which is shown in Figure 4, is described here as a typical case. The packing mode of $C_{18}MImAF_6$ is described as a layered structure of polar and non-polar domains. The sheets consisting of the imidazolium headgroups and TaF_6^- anions (polar domains) are separated by interdigitated alkyl chains (non-polar domains) tilted relative to the polar domain (Figure 4(a)). The polar domain is made up of a double layer of a NaCl-type ion configuration, where one of the two layers is not lying on the other in the ideal

manner for a NaCl-type structure (Figure 4 (b)). The alkyl chain keeps a trans conformation from C8 to C23 and is bent near the imidazolium ring like a spoon (Figures 4 (c) and (d)), as was reported for $C_{12}MImPF_6$ and $C_{14}MImPF_6$.[14-15]

Crystal structures were also determined at 25 and 55 °C for all the five $C_{18}MImAF_6$ salts (see Figure 4 (d) for the unit cells). Although the overall cation-anion configurations at –100, 25, and 55 °C are similar to each other, the carbon atoms in the octadecyl chain are significantly disordered near the imidazolium ring at 25 and 55 °C and it was hard to solve the structure completely. The atomic displacement parameters become large as the temperature increases, especially for the C7, C8, C9, and C10 atoms. The positions of fluorine atoms in AF_6^- are slightly disordered at 25 and 55 °C, but the structure of AF_6^- was solved as a non-disordered regular octahedron in this study because the degree of its disordering was not significant. Although a similar structural change was reported for $C_{14}MImPF_6$ between –98 to 27 °C, the present diffraction studies at 25 and 55 °C propose a more detailed model. The best model obtained is shown as a schematic illustration in Figure 5. The octadecyl chain which has a bent conformation at –100 °C adopts an all-trans conformation at 55 °C, whereas the electron density map obtained at 25 °C suggests mixing of the all-trans and bent conformation. This result suggests that the trans conformation is preferred near the melting point and the ratio of the trans conformation to the bent conformation becomes large as the temperature increases. The solid-solid phase transition observed in the crystalline phase seems to result from such structural changes. It is notable that the ratios of the two conformers at 25 °C are different in the five cases and the solid-solid transition temperature is dependent on the anion size. Packing of the ions at low temperatures is tighter compared to those at or above room temperature, which is reflected to the increase in tilted angle of the

alkyl chains with regard to the polar sheet. Since the imidazolium head groups and the anions are connected by ionic interaction in the polar sheet, and the alkyl chains are connected with each other by van der Waals interaction in the nonpolar sheet, such an increase of tilted angle leads to a conformation change of C7, C8, C9, and C10 atoms.

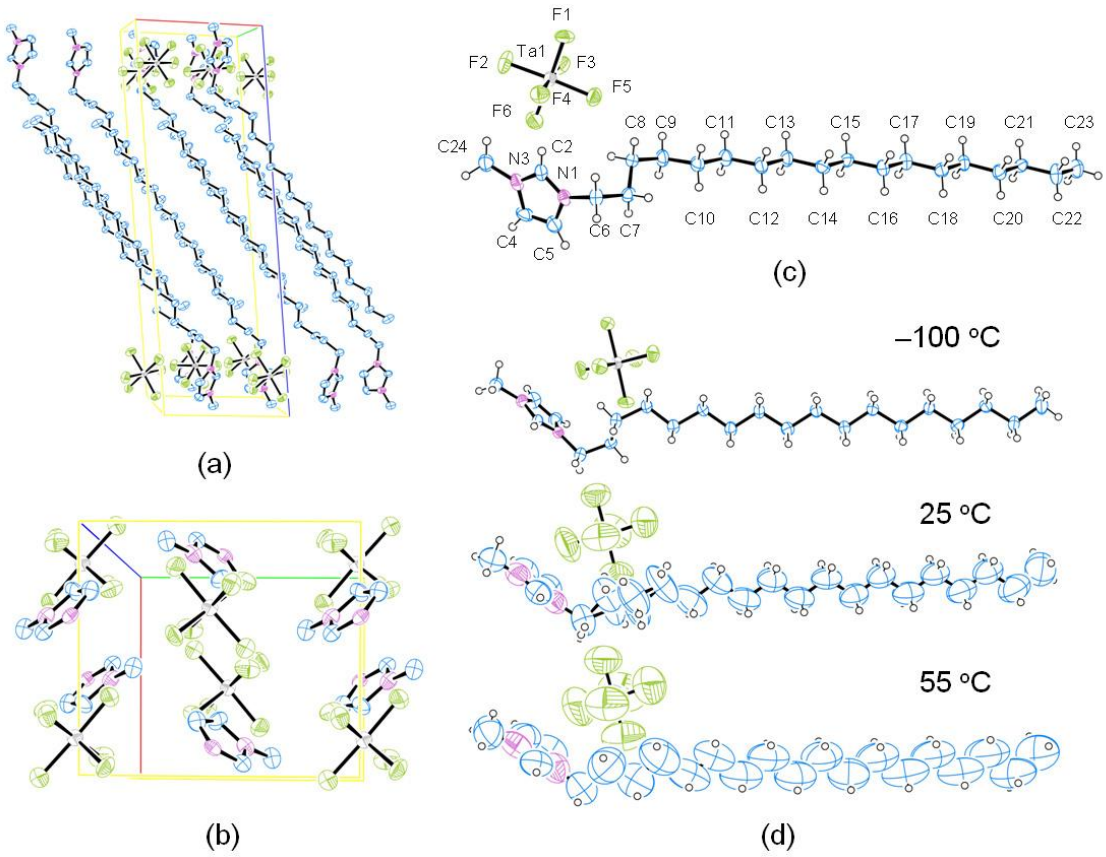

Figure 4 Crystal structure of $C_{18}MImTaF_6$. (a) Packing diagram at –100 °C, (b) configuration of the imidazolium headgroup and TaF_6^- in the polar region at –100 °C, (c) asymmetric unit with atom numbering scheme at –100 °C, (d) structures of $C_{18}MIm^+$ and TaF_6^- at –100, 25, and 55 °C.

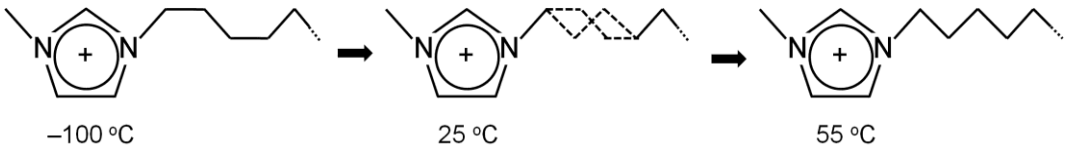

Figure 5 Schematic drawing of structural changes for $C_{18}MImAF_6$ at −100, 25, and 55 °C.

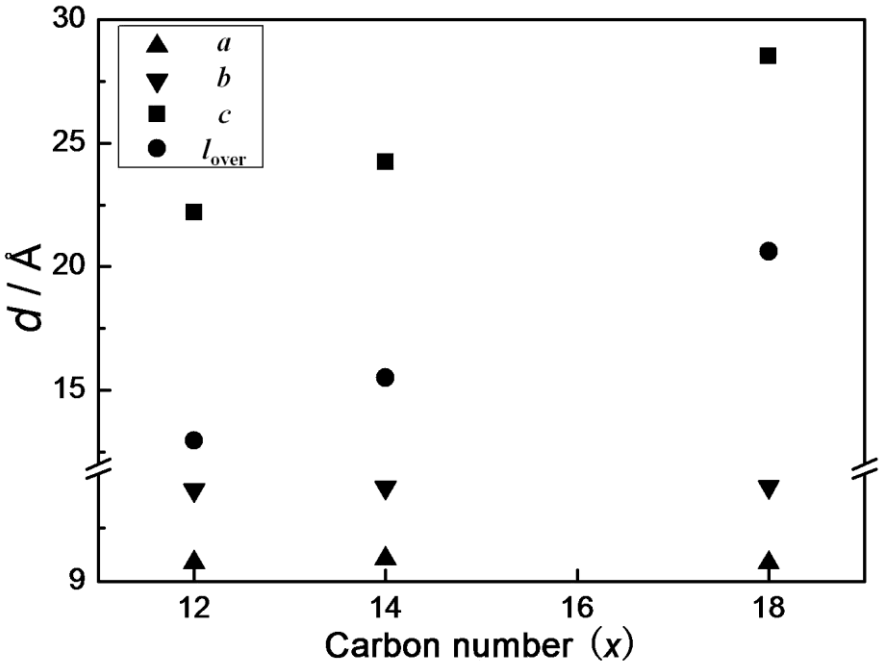

Figure 6 Cell parameters (*a*, *b*, and *c*) for $C_{12}MImPF_6$, $C_{14}MImPF_6$, and $C_{18}MImPF_6$. The overlapped alkyl chain length (l_{over}) is also plotted (see Table S3 for calculation of l_{over}).

Sharper changes of some cell parameters, especially β, are observed between 25 and 55 °C (Table S1 and S2, Supporting Information) compared with those between –100 and 25 °C, which are in good accordance with the crystal-crystal phase transition temperatures observed from DSC results. Comparison of the crystal structures between $C_{12}MImPF_6$, $C_{14}MImPF_6$, and $C_{18}MImPF_6$ also gives interesting information on cell parameters (Note: The data collection temperatures are –150 °C for $C_{12}MImPF_6$,[14] –98 °C for $C_{14}MImPF_6$,[15] and –100 °C for $C_{18}MImPF_6$). The *a* and *b* cell parameters, corresponding to the NaCl-type layer, do not show a significant change, whereas the *c* cell parameter increases as the alkyl chain length increases (Figure 6), and the alkyl-alkyl interdigitated part always roughly starts from C9 regardless of the alkyl chain length. The difference in the overlapped alkyl chain length (12.947 Å, 15.497 Å, and 20.617 Å for x = 12, 14, and 18, Table S3, Supporting Information) directly corresponds to the number of the methylene group

added.

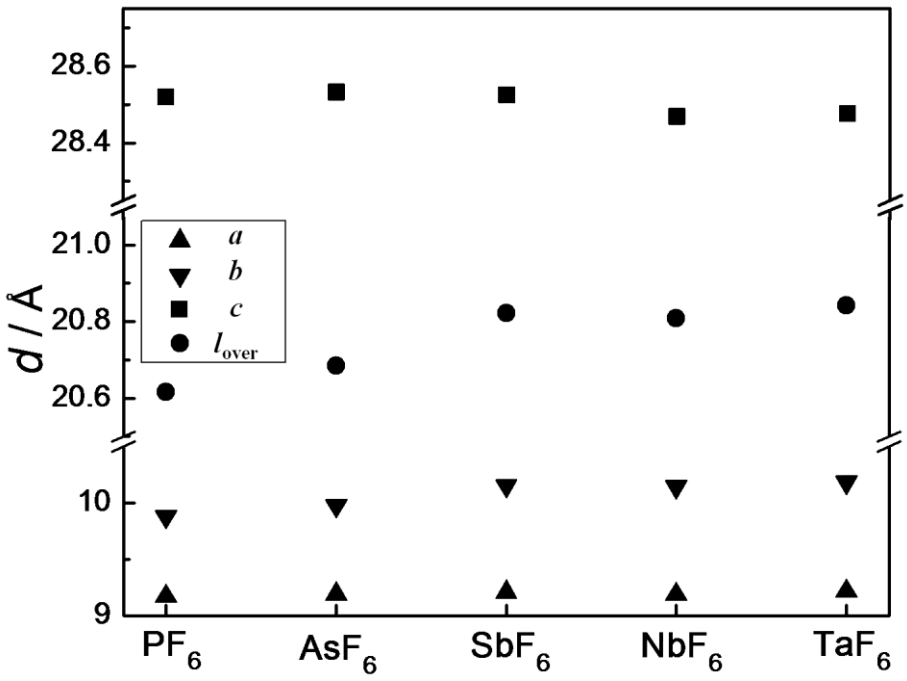

Figure 7 Cell parameters (*a*, *b*, and *c*) for $C_{18}MImAF_6$ (A = P, As, Sb, Nb, and Ta) at –100 °C. The overlapped alkyl chain length (l_{over}) is also plotted (see Table S4 for calculation of l_{over}).

Figure 7 shows the cell parameters (*a*, *b*, and *c*) of $C_{18}MImAF_6$ (A = P, As, Sb, Nb, and Ta) at –100 °C. With increasing the anion size, the *a* parameter shows a very small change and the *b* parameter slightly increases, leading to an increase of the area in the ionic sheets. The *c* parameter remains nearly constant for the PF_6, AsF_6, and SbF_6 salts and becomes smaller for the NbF_6 and TaF_6 salts, in spite of the larger sizes of NbF_6^- and TaF_6^-. The value of $c \times \sin\beta$, which is the distance between the layers, decreases with increasing anion size (Table S4, Supporting Information), with the only exception of SbF_6. The overlapped alkyl chain length also increases with increasing anion size (Figure 7 and Table S4, Supporting Information). This observation means that the alkyl chains interdigitate more deeply as the anion becomes larger, which is probably due to the weaker cation-anion interaction and the larger alkyl chain interspacing caused by the larger anion.

Table 2 The C−H···F interaction geometries (Å, °) in $C_{18}MImTaF_6$.

D–H···*A*	*D*–H	H···*A*	*D*···*A*	∠*D*–H···*A*
C2–H2^{i}···F1	0.930	2.598	2.978	105.07
C4–H4^{ii}···F1	0.930	2.586	3.326	136.80
C24–H24a^{iv}···F1	0.960	2.605	3.113	113.35
C4–H4^{ii}···F2	0.930	2.633	3.425	143.32
C5–H5^{v}···F3	0.930	2.357	3.211	152.51
C6–H6b^{i}···F4	0.970	2.634	3.440	140.65
C8–H8a^{iv}···F4	0.970	2.700	3.352	124.96
C23–H23b^{iii}···F4	0.960	2.691	3.620	163.06
C2–H2^{iv}···F5	0.930	2.458	3.093	125.59
C6–H6a^{v}···F6	0.970	2.462	3.398	161.92
C7–H7a···F6	0.970	2.615	3.579	172.15

Symmetry codes: (i) –1+*x*, *y*, *z*; (ii) –*x*, –*y*, –*z*; (iii) –1–*x*, –*y*, 1–*z*; (iv) –1/2+*x*, –1/2–*y*, *z*; (v) –1/2+*x*, 1/2–*y*, *z*.

Table 2 lists C–H···F interactions for $C_{18}MImTaF_6$. All F atoms are involved in short contacts (below the sum of van der Waals radii) with H atoms of the imidazolium ring (F1, F2, F3, and F5) or that of the alkyl side-chains (F1, F4, F6). Bifurcation of the C–H···F bonds is observed for H atoms (H2 and H4) which interact with two F atoms (F1 and F5, F1 and F2, respectively) of TaF_6^-. Similar phenomena were also observed for the other $C_{18}MImAF_6$ salts (A = P, As, Sb, and Nb).

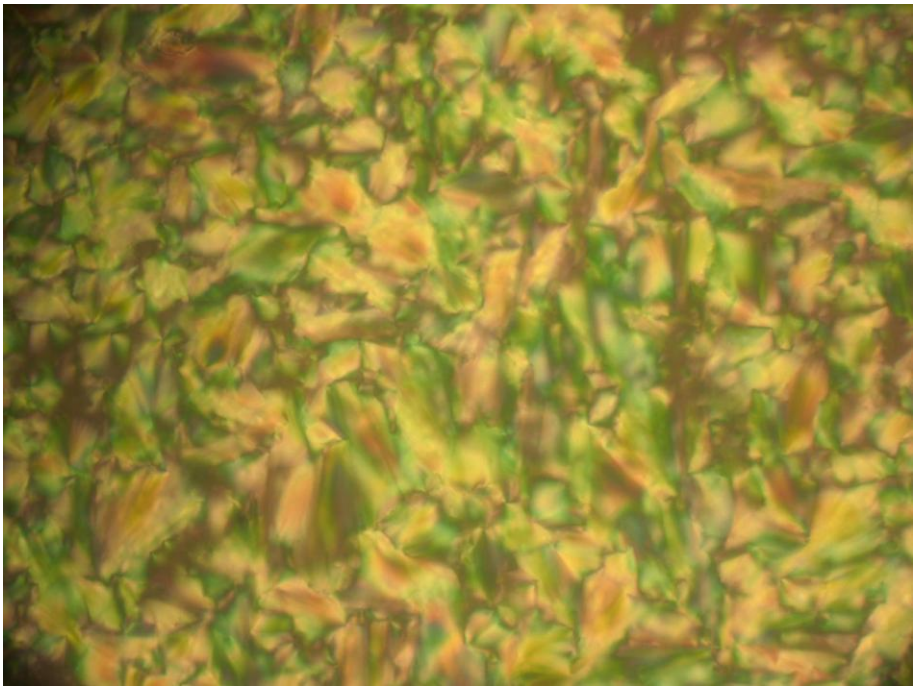

Figure 8 Polarized optical microscopic texture of $C_{18}MImTaF_6$ at 100 °C.

Figure 8 shows a polarized optical microscopic (POM) texture of $C_{18}MImTaF_6$

which is typical of all the C_xMImAF_6 ILCs (see Figures S12-S14, Supporting Information for the other salts) and characterized by spontaneous formation of smooth fan-like or focal conic textures. The broken fan-like texture which is indicative of the smectic C mesophase was not observed in the liquid crystalline mesophase on cooling from the isotropic phase to the crystalline mesophase, suggesting the absence of the smectic C mesophase in these systems.[24-25] These results of POM combined with the XRD study below suggest that the liquid crystalline mesophase of C_xMImAF_6 ILCs is assigned to smectic A mesophase.[1,11,13-14,18] Such an enantiotropic smectic A liquid crystalline mesophase was also observed for other 1-alkyl-3-methylimidazolium ILCs in previous reports, since the large cation dominates formation of the smectic layer.[11-14,18]

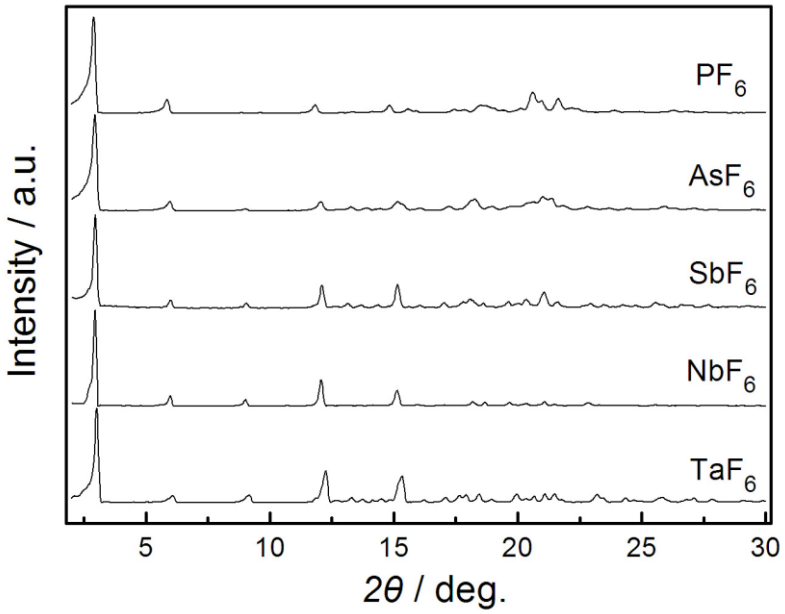

Figure 9 X-ray diffraction patterns for $C_{18}MImAF_6$ (A = P, As, Sb, Nb, and Ta) in the crystalline phase (40 °C).

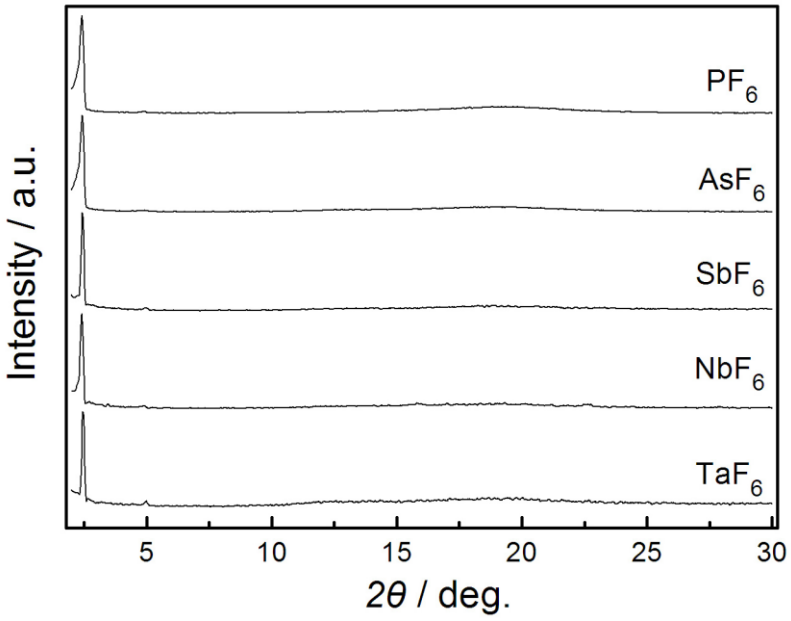

Figure 10 X-ray diffraction patterns for $C_{18}MImAF_6$ (A = P, As, Sb, Nb, and Ta) in the liquid crystalline mesophase (100 °C).

Figures 9 and 10 show the XRD patterns ($2° < 2\theta < 30°$) of the crystalline phase and liquid crystalline mesophase for $C_{18}MImAF_6$, respectively. In both the phases, sharp peaks are observed in the low-angle region, indicating formation of layered structures, and no peak was found in the region lower than 2.0°. The similar crystal structures of $C_{18}MImAF_6$ result in the similar 2θ-angle for the sharp peaks in the XRD pattern of the crystalline phase (see Figures S15 and S16, Supporting Information, for $C_{14}MImAF_6$ and $C_{16}MImAF_6$). Absence of additional peaks in the high-angle region in the cases of liquid crystals suggests the loss of positional ordering within the layer plane, which fits the characteristics of smectic A mesophase. Small peaks around 5.0° were observed for $C_{18}MImAF_6$ and $C_{16}MImPF_6$, and were indexed as the (002) diffraction of the smectic layers (Figure 10 and S17). Measurements of the patterns of the liquid crystalline mesophase were difficult for $C_{16}MImSbF_6$, $C_{16}MImNbF_6$, and $C_{16}MImTaF_6$ due to the relatively narrow temperature range of their mesophases.

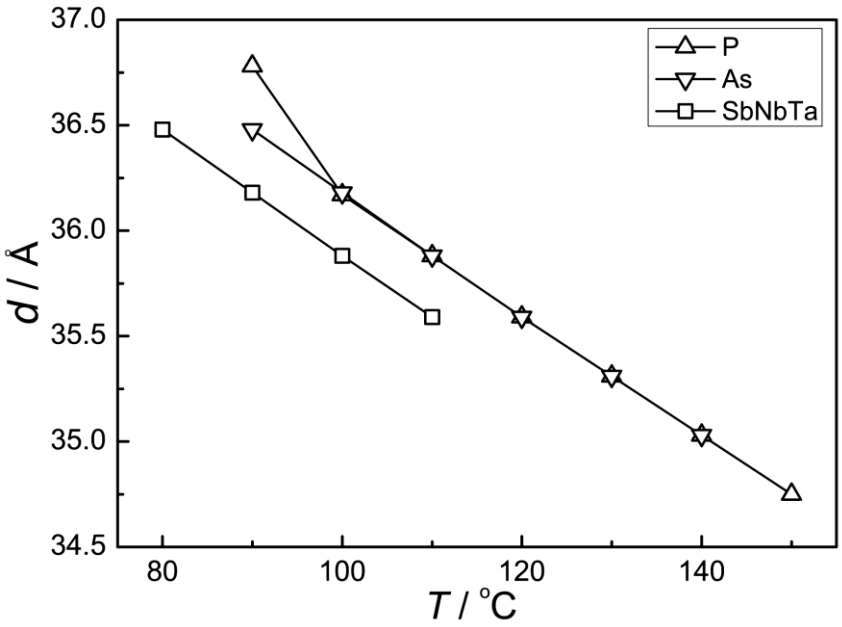

Figure 11 Layer spacings of $C_{18}MImAF_6$ (A = P, As, Sb, Nb, and Ta) in the liquid crystalline mesophase.

Figure 11 shows the layer spacing (d) of $C_{18}MImAF_6$ in the liquid crystalline mesophase as a function of temperature. The layer spacing d is found to satisfy $l < d < 2l$, where l is the fully extended length of the cation, which indicates an interdigitated bilayer structure is formed in the smectic A liquid crystalline mesophase (smectic A_2).[12,18] The layer spacing decreases with increase in temperature, which is also indicative of smectic A_2 mesophase.[12,18] To our knowledge, all the 1-alkyl-3-methylimidazolium ILCs known today show the same type of liquid crystalline mesophase of smectic A_2, since the bulky cation is much larger than the anion and dominates the type of mesophase for such ILCs.[12-14,18] The layer spacing for PF_6^- and AsF_6^- is larger than that for SbF_6^-, NbF_6^-, and TaF_6^-, which can be explained by changes in the cation-anion interactions within the polar region. The bilayer structure interdigitates more deeply with decreasing cation-anion interaction due to the increase of thermal mobility of the cations, leading to the decrease of the layer spacing. Increase of the AF_6^- anion size results in the longer cation-anion distance and

weaker cation-anion interactions, which facilitates the interdigitation of the alkyl chains and leads to the smaller layer spacing. The same trend observed in the crystal structure as shown above also supports this explanation. Similar phenomena were also observed for $C_{16}MImPF_6$ and $C_{16}MImAsF_6$ (Figure S18, Supporting Information).

Conclusions

Thermal and structural properties of 1-alkyl-3-methylimidazolium hexafluorocomplex salts, C_xMImAF_6 (x = 14, 16, and 18, A = P, As, Sb, Nb, and Ta), were investigated. These salts exhibit a liquid crystalline mesophase with a smectic A structure and the temperature range of the mesophase increases with increasing alkyl chain length or decreasing anion size, suggesting both the van der Waals interaction between the alkyl chains and the electrostatic interaction between the imidazolium headgroup and the anion have an effect on stabilization of the liquid crystalline mesophase. X-ray single crystallography revealed that all the five $C_{18}MImAF_6$ salts have the same layered structure where the nonpolar layer of interditated alkyl chains and the polar layer of the imidazolium head group and the anion alternate with each other. The octadecyl chain of $C_{18}MIm^+$ in the $C_{18}MImAF_6$ crystal structure at –100 °C has a bent structure, which changes into a trans conformation as temperature increases. The layer spacing (d) in the liquid crystalline mesophases satisfies the relation of $l < d < 2l$ (l is the fully extended length of the cation) and monotonously decreases with increasing temperature, indicative of a smectic A_2 interdigitated bilayer structure. The layer spacing in mesophase decreases with increasing anion size, due to the decrease of cation-anion interactions within the polar region.

Experimental Section

Apparatus and Materials. Volatile materials were handled in a vacuum line constructed of SUS316 stainless steel and PFA (tetrafluoroethylene-perfluoroalkylvinylether copolymer). Nonvolatile materials were handled under a dry Ar atmosphere in a glove box. Acetone (Wako Chemicals, 99.5%) and dichloromethane (Aldrich, 99.8%) were used as purchased. The 1-alkyl-3-methylimidazolium chlorides, C_xMImCl (x = 14, 16, and 18), were prepared by reactions of 1-methylimidazole (Aldrich, 99%) and equimolar quantities of the corresponding chloroalkanes (1-chlorotetradecane (Aldrich, 98%), 1-chlorohexadecane (Wako Chemicals, 95%), 1-chlorooctadecane (Wako Chemicals, 95%)) at temperatures between 70 and 100 °C for several days. Purification of the chlorides was performed by dissolving the chloride salts in acetonitrile (dehydrated, Wako Chemicals, 99%) and then precipitating from the solution by adding ethyl acetate (dehydrated, Wako Chemicals, 99.5%). The hexafluorocomplex salts (KPF_6 (Wako Chemicals), $NaAsF_6$ (Aldrich), $KSbF_6$ (Aldrich, 99%)) were used as purchased. Potassium fluoride (Wako chemicals, 99%) was dried under vacuum at 180 °C for a few days before use. Anhydrous HF (Daikin Industries) was dried over K_2NiF_6 prior to use. Niobium pentafluoride (NbF_5, Aldrich, 99%) and tantalum pentafluoride (TaF_5, Furuuchi Chemical Corp., 99.5%) were used as purchased. The two potassium salts, $KNbF_6$ and $KTaF_6$, were prepared by the reaction of KF and the corresponding metal pentafluorides in HF according to the previous report.[23,26] A white powder sample obtained was dried under dynamic vacuum at 70 °C.

Synthesis of C_{14}MImPF$_6$. The two starting materials, C_{14}MImCl (3.150g, 10.00 mmol) and KPF_6 (2.024 g, 11.00 mmol), were dissolved in water (30 mL), and the mixture was stirred vigorously overnight. A slightly excess amount of KPF_6 was used for the thorough removal of Cl^-. The solid product was separated from the mixture by

centrifugation and the remaining water-soluble species were washed with water several times. Testing for the presence of residual chloride impurities in the water phase with 1M $AgNO_3$ aqueous solution gave no precipitation of AgCl. The product was dried under vacuum at room temperature and then at 80 °C (3.574 g, 8.420 mmol). Anal. Calcd. for $C_{18}H_{35}N_2F_6P_1$: C, 50.94; H, 8.25; N, 6.60; F, 26.89. Found: C, 50.77; H, 8.34; N, 6.72; F, 26.94. Raman (frequency/cm^{-1} (relative intensity)): 741(s) (PF_6^-, ν_1), 566(w) (PF_6^-, ν_2), 471(m) (PF_6^-, ν_5). IR (frequency/cm^{-1} (relative intensity)): 847(w) (PF_6^-, ν_3), 556(s) (PF_6^-, ν_4) (See S1-S6 for the vibrational spectra of C_xMImAF_6). Here, s, m, and w for relative intensity denote strong, medium, and weak, respectively.

Synthesis of C_{16}MImPF_6. The same procedure as for C_{14}MImPF_6 was used. Anal. Calcd. for $C_{20}H_{39}N_2F_6P_1$: C, 53.10; H, 8.63; N, 6.19; F, 25.22. Found: C, 52.98; H, 8.55; N, 6.35; F, 25.44. Raman (frequency/cm^{-1} (relative intensity)): 742(s) (PF_6^-, ν_1), 565(w) (PF_6^-, ν_2), 471(m) (PF_6^-, ν_5). IR (frequency/cm^{-1} (relative intensity)): 847(w) (PF_6^-, ν_3), 554(s) (PF_6^-, ν_4).

Synthesis of C_{18}MImPF_6. The same procedure as for C_{14}MImPF_6 was used. Anal. Calcd. for $C_{22}H_{43}N_2F_6P_1$: C, 55.00; H, 8.96; N, 5.83; F, 23.75. Found: C, 54.76; H, 9.01; N, 5.94; F, 23.67. Raman (frequency/cm^{-1} (relative intensity)): 741(s) (PF_6^-, ν_1), 568(w) (PF_6^-, ν_2), 471(m) (PF_6^-, ν_5). IR (frequency/cm^{-1} (relative intensity)): 845(w) (PF_6^-, ν_3), 554(s) (PF_6^-, ν_4).

Synthesis of C_{14}MImAsF_6. The same procedure as for C_{14}MImPF_6 was used. Anal. Calcd. for $C_{18}H_{35}N_2F_6As_1$: C, 46.15; H, 7.48; N, 5.98; F, 24.36. Found: C, 46.06; H, 7.42; N, 5.96; F, 24.18. Raman (frequency/cm^{-1} (relative intensity)): 678(s) (AsF_6^-, ν_1), 575(w) (AsF_6^-, ν_2), 368(m) (AsF_6^-, ν_5). IR (frequency/cm^{-1} (relative intensity)): 693(m) (AsF_6^-, ν_3).

Synthesis of C_{16}MImAsF_6. The same procedure as for C_{14}MImPF_6 was used. Anal. Calcd. for $C_{20}H_{39}N_2F_6As_1$: C, 48.39; H, 7.86; N, 5.65; F, 22.98. Found: C, 48.36; H, 7.65; N, 5.68; F, 23.21. Raman (frequency/cm^{-1} (relative intensity)): 678(s) (AsF_6^-, ν_1), 573(w) (AsF_6^-, ν_2), 369(m) (AsF_6^-, ν_5). IR (frequency/cm^{-1} (relative intensity)): 695(m) (AsF_6^-, ν_3).

Synthesis of C_{18}MImAsF_6. The same procedure as for C_{14}MImPF_6 was used. Anal. Calcd. for $C_{22}H_{43}N_2F_6As_1$: C, 50.38; H, 8.21; N, 5.34; F, 21.76. Found: C, 50.09; H, 8.20; N, 5.37; F, 21.74. Raman (frequency/cm^{-1} (relative intensity)): 678(s) (AsF_6^-, ν_1), 573(w) (AsF_6^-, ν_2), 368(m) (AsF_6^-, ν_5). IR (frequency/cm^{-1} (relative intensity)): 698(s) (AsF_6^-, ν_3).

Synthesis of C_{14}MImSbF_6. The same procedure as for C_{14}MImPF_6 was unsuccessful for the synthesis of C_{14}MImSbF_6 since addition of C_{14}MImCl and KSbF_6 into water gave a gel-like solution, making the separation of the product difficult. Instead of this method, the following procedure was used for the SbF_6 salts. The two starting materials, C_{14}MImCl (3.150 g, 10.00 mmol) and KSbF_6 (2.886 g, 10.50 mmol), were dissolved in 30 mL of acetone, and the mixture was stirred vigorously overnight. The solution was separated from the mixture by centrifugation, and the acetone was removed under vacuum at room temperature. Testing for the presence of residual chloride impurities with a 1M $AgNO_3$ aqueous solution gave no precipitation of AgCl. The product was dissolved in 20 mL of dichloromethane and the mixture was stirred vigorously overnight. The dichloromethane solution was separated from the precipitate (probably the potassium salt) by centrifugation, and dichloromethane was removed under vacuum at room temperature initially and then at 80 °C for 3 days. Anal. Calcd. for $C_{18}H_{35}N_2F_6Sb_1$: C, 41.94; H, 6.80; N, 5.44; F, 22.14. Found: C, 41.84; H, 6.76; N, 5.44; F, 21.94. Raman (frequency/cm^{-1} (relative intensity)): 645(s) (SbF_6^-,

ν_1), 280(m) (SbF_6^-, ν_5). IR (frequency/cm^{-1} (relative intensity)): 654(m) (SbF_6^-, ν_3).

Synthesis of C_{16}MImSbF$_6$. The same procedure as for C_{14}MImSbF$_6$ was used. Anal. Calcd. for $C_{20}H_{39}N_2F_6Sb_1$: C, 44.20; H, 7.18; N, 5.16; F, 20.99. Found: C, 44.20; H, 7.14; N, 5.25; F, 20.88. Raman (frequency/cm^{-1} (relative intensity)): 645(s) (SbF_6^-, ν_1), 570(w) (SbF_6^-, ν_2), 280(m) (SbF_6^-, ν_5). IR (frequency/cm^{-1} (relative intensity)): 656(m) (SbF_6^-, ν_3).

Synthesis of C_{18}MImSbF$_6$. The same procedure as for C_{14}MImSbF$_6$ was used. Anal. Calcd. for $C_{22}H_{43}N_2F_6Sb_1$: C, 46.23; H, 7.53; N, 4.90; F, 19.96. Found: C, 46.07; H, 7.37; N, 4.86; F, 19.72. Raman (frequency/cm^{-1} (relative intensity)): 645(s) (SbF_6^-, ν_1), 571(w) (SbF_6^-, ν_2), 280(m) (SbF_6^-, ν_5). IR (frequency/cm^{-1} (relative intensity)): 654(m) (SbF_6^-, ν_3).

Synthesis of C_{14}MImNbF$_6$. The same procedure as for C_{14}MImSbF$_6$ was used. Anal. Calcd. for $C_{18}H_{35}N_2F_6Nb_1$: C, 44.44; H, 7.20; N, 5.76; F, 23.46. Found: C, 44.56; H, 7.37; N, 5.79; F, 23.26. Raman (frequency/cm^{-1} (relative intensity)): 681(s) (NbF_6^-, ν_1), 285(m) (NbF_6^-, ν_5). IR (frequency/cm^{-1} (relative intensity)): 608(w) (NbF_6^-, ν_3).

Synthesis of C_{16}MImNbF$_6$. The same procedure as for C_{14}MImSbF$_6$ was used. Anal. Calcd. for $C_{20}H_{39}N_2F_6Nb_1$: C, 46.69; H, 7.59; N, 5.45; F, 22.18. Found: C, 46.90; H, 7.76; N, 5.50; F, 21.92. Raman (frequency/cm^{-1} (relative intensity)): 681(s) (NbF_6^-, ν_1), 284(m) (NbF_6^-, ν_5). IR (frequency/cm^{-1} (relative intensity)): 604(w) (NbF_6^-, ν_3).

Synthesis of C_{18}MImNbF$_6$. The same procedure as for C_{14}MImSbF$_6$ was used. Anal. Calcd. for $C_{22}H_{43}N_2F_6Nb_1$: C, 48.71; H, 7.93; N, 5.17; F, 21.03. Found: C, 49.00; H, 8.07; N, 5.26; F, 20.92. Raman (frequency/cm^{-1} (relative intensity)): 681(s) (NbF_6^-, ν_1), 285(m) (NbF_6^-, ν_5). IR (frequency/cm^{-1} (relative intensity)): 606(m) (NbF_6^-, ν_3).

Synthesis of C_{14}MImTaF$_6$. The same procedure as for C_{14}MImSbF$_6$ was used. Anal. Calcd. for $C_{18}H_{35}N_2F_6Ta_1$: C, 37.63; H, 6.10; N, 4.88; F, 19.86. Found: C, 37.66; H,

6.02; N, 4.88; F, 19.60. Raman (frequency/cm^{-1} (relative intensity)): 693(s) (TaF_6^-, ν_1), 290(m) (TaF_6^-, ν_5). IR (frequency/cm^{-1} (relative intensity)): 573(w) (TaF_6^-, ν_3).

Synthesis of C_{16}MImTaF_6. The same procedure as for C_{14}MImSbF_6 was used. Anal. Calcd. for $C_{20}H_{39}N_2F_6Ta_1$: C, 39.87; H, 6.48; N, 4.65; F, 18.94. Found: C, 39.70; H, 6.25; N, 4.70; F, 19.09. Raman (frequency/cm^{-1} (relative intensity)): 693(s) (TaF_6^-, ν_1), 287(m) (TaF_6^-, ν_5). IR (frequency/cm^{-1} (relative intensity)): 575(w) (TaF_6^-, ν_3).

Synthesis of C_{18}MImTaF_6. The same procedure as for C_{14}MImSbF_6 was used. Anal. Calcd. for $C_{22}H_{43}N_2F_6Ta_1$: C, 41.90; H, 6.83; N, 4.44; F, 18.10. Found: C, 41.88; H, 6.82; N, 4.50; F, 17.87. Raman (frequency/cm^{-1} (relative intensity)): 693(s) (TaF_6^-, ν_1), 287(m) (TaF_6^-, ν_5). IR (frequency/cm^{-1} (relative intensity)): 576(m) (TaF_6^-, ν_3).

Spectroscopic and Thermal Analyses. Infra-red spectra were obtained by FTS-165 (Bio-Rad Laboratories). The samples were sandwiched between a pair of AgCl windows fixed in a stainless airtight cell under dry Ar. Raman spectra were obtained by FTS-175C (Bio-Rad Laboratories) using the 1064 nm line of a Nd:YAG laser as the excitation line. The samples for Raman spectroscopy were loaded in Pyrex glass tubes under dry Ar and sealed with a plastic cap. Thermogravimetric and DSC analyses were performed under a dry Ar gas flow using Shimadzu DTG-60H and Shimadzu DSC-60, respectively, at the scan rate of 5 °C min^{-1}. The sample was placed in a Ni open cell for TG analysis and in an aluminum sealed cell for DSC analysis. Polarized optical microscopy was carried out using a VHX digital microscope (Keyence, Co.) under cross-polarized light at ×100 magnification**.** The sample was placed in a transparent cell made of sapphire and covered with a piece of glass substrate. The temperature was controlled by TS1500 hot stage unit (Japan High Tech Co., Ltd.).

X-Ray Diffraction Analyses. a. Powder Diffraction. X-ray diffraction was

performed using a Rigaku Ultima IV diffractometer (Cu-Kα, λ = 1.542 Å). The output power was set as 40 kV-40 mA. The data were recorded in the 2θ ranges of 2–30° (scanning rate of 2° per minute) with a step of 0.02°. The sample was sealed in a vacuum cell. The heating and cooling rate of 5 °C min^{-1} was used.

b. Single-Crystal Diffraction. Crystals of $C_{18}MImAF_6$ (A = P, As, Sb, Nb, and Ta) were grown by slow evaporation of the solvent from the acetone (A = P, As, Sb, Ta) or dichloromethane (A = Nb) solution. Suitable crystals of $C_{18}MImAF_6$ (A = P, As, Sb, and Ta) were fixed on a glass rod with perfluoro polyether oil (fomblin YL VAC 06\6) and centered on an X-ray diffractometer (R-axis Rapid II, Rigaku controlled by the program RAPID AUTO 2.40) equipped with an imaging plate area detector (using the program RAPID XRD 2.3.3) and graphite-monochromated Mo Kα radiation (0.71073 Å). The crystal of $C_{18}MImNbF_6$ was transferred into a quartz capillary (0.5 mm o.d., dried under a vacuum at 500 °C) under a dry Ar atmosphere. The capillary was tentatively plugged with vacuum grease and sealed using an oxygen burner. Data collection was performed at –100, 25, and 55 °C. The measurements consisted of 12 ω scans (130-190°, 5°/frame) at the fixed φ (30°) and χ (45°) angles and 32 ω scans (0-160°, 5°/frame) at the fixed φ (180°) and χ (45°) angles for $C_{18}MImPF_6$, $C_{18}MImAsF_6$, and $C_{18}MImSbF_6$, and 20 ω scans (130-190°, 3°/frame) at the fixed φ (30°) and χ (45°) angles and 54 ω scans (0-162°, 3°/frame) at the fixed φ (180°) and χ (45°) angles for $C_{18}MImNbF_6$ and $C_{18}MImTaF_6$. The exposure time was 300 s deg^{-1}. Integration, scaling and absorption corrections were performed using RAPID AUTO 2.40. The structure was solved using SIR-92 and refined by SHELXL-97 linked to Win-GX. Anisotropic displacement factors were introduced for all atoms except for hydrogen. The crystallographic data and refinement results of $C_{18}MImAF_6$ are summarized in Table 3.

Table 3 Summary of crystal data and refinement results for $C_{18}MImAF_6$ (A = P, As, Sb, Nb, and Ta) at –100 °C.

	P	As	Sb	Nb	Ta
Formula	$C_{22}H_{43}N_2F_6P$	$C_{22}H_{43}N_2F_6As$	$C_{22}H_{43}N_2F_6Sb$	$C_{22}H_{43}N_2F_6Nb$	$C_{22}H_{43}N_2F_6Ta$
Fw	480.55	524.50	571.34	542.49	630.53
crystal size, mm	0.80×0.30×0.05	0.70×0.20×0.05	0.75×0.30×0.03	0.70×0.30×0.05	0.43×0.13×0.04
T/°C	–100	–100	–100	–100	–100
crystal system	monoclinic	monoclinic	monoclinic	monoclinic	monoclinic
space group	$P2_1/a$	$P2_1/a$	$P2_1/a$	$P2_1/a$	$P2_1/a$
a/Å	9.1715(7)	9.1894(2)	9.2091(3)	9.1865(5)	9.2100(3)
b/Å	9.8807(8)	9.9779(3)	10.1539(5)	10.1457(7)	10.1744(3)
c/Å	28.520(2)	28.5321(7)	28.5250(10)	28.4689(15)	28.4495(11)
β/°	95.707(2)	96.0148(7)	96.2477(10)	96.1335(16)	96.1688(11)
V/Å^3	2571.7(3)	2601.74(12)	2651.47(18)	2638.2(3)	2650.46(15)
Z	4	4	4	4	4
ρ_{calcd}/g cm^{-3}	1.241	1.339	1.431	1.366	1.576
F(000)	1032	1104	1176	1136	1264
μ/mm^{-1}	0.161	1.360	1.093	0.509	4.188
λ/Å	0.71073	0.71073	0.71073	0.71073	0.71073
reflns collected/unique	22634/5864	24782/5884	25221/6035	15005/5954	11776/3944
$R_1(F_o)^a$	0.0465	0.0418	0.0262	0.0470	0.0349
$wR_2(F_o^2)^b$	0.1059	0.0981	0.0656	0.1125	0.1100
R_{int}	0.0556	0.0452	0.0294	0.0536	0.0402

^{a} $R_1 = \sum||F_o| - |F_c|| / \sum|F_o|$ for $I > 2\sigma(I)$. ^{b} $wR_2 = \{\sum[w(F_o^2 - F_c^2)^2] / \sum[w(F_o^2)^2]\}^{1/2}$ for $I > 2\sigma(I)$.

Acknowledgments

This work was financially supported by the Grant-in-Aid for Scientific Research of Japan Society for the Promotion of Science, # 20246140.

References

1 K. Binnemans, *Chem. Rev.*, 2005, **105**, 4148–4204.
2 M. Yoshio, T. Kagata, K. Hoshino, T. Mukai, H. Ohno and T. Kato, *J. Am. Chem. Soc.*, 2006, **128**, 5570–5577.
3 M. Yoshio, T. Mukai, H. Ohno and T. Kato, *J. Am. Chem. Soc.*, 2004, **126**, 994–995.
4 H. Shimura, M. Yoshio, K. Hoshino, T. Mukai, H. Ohno and T. Kato, *J. Am. Chem. Soc.*, 2008, **130**, 1759–1765.
5 M. Yoshio, T. Mukai, K. Kanie, M. Yoshizawa, H. Ohno and T. Kato, *Adv. Mater.*, 2002, **14**, 351–354.
6 T. Mukai, M. Yoshio, T. Kato, M. Yoshizawa and H. Ohno, *Chem. Commun.*, 2005, 1333–1335.
7 N. Yamanaka, R. Kawano, W. Kubo, T. Kitamura, Y. Wada, M. Watanabe and S. Yanagida, *Chem. Commun.*, 2005, 740–742.
8 T. Welton, *Chem. Rev.*, 1999, **99**, 2071–2083.
9 T. Kato, *Science*, 2002, **295**, 2414–2418.
10 K. Goossens, P. Nockemann, K. Driesen, B. Goderis, C. Görller-Walrand, K. Van Hecke, L. Van Meervelt, E. Pouzet, K. Binnemans and T. Cardinaels, *Chem. Mater.*, 2008, **20**, 157–168.
11 C. J. Bowlas, D. W. Bruce and K. R. Seddon, *Chem. Commun.*, 1996, 1625–1626.
12 A. E. Bradley, C. Hardacre, J. D. Holbrey, S. Johnston, S. E. J. McMath and M. Nieuwenhuyzen, *Chem. Mater.*, 2002, **14**, 629–635.
13 J. D. Holbrey and K. R. Seddon, *J. Chem. Soc. Dalton Trans.*, 1999, 2133–2139.
14 C. M. Gordon, J. D. Holbrey, A. R. Kennedy and K. R. Seddon, *J. Mater. Chem.*, 1998, **8**, 2627–2636.
15 J. De Roche, C. M. Gordon, C. T. Imrie, M. D. Ingram, A. R. Kennedy, F. Lo Celso and A. Triolo, *Chem. Mater.*, 2003, **15**, 3089–3097.
16 W. M. Reichert, J. D. Holbrey, R. P. Swatloski, K. E. Gutowski, A. E. Visser, M. Nieuwenhuyzen, K. R. Seddon and R. D. Rogers, *Cryst. Growth Des.*, 2007, **7**, 1106–1114.
17 K. Nakamoto, *Infrared and Raman Spectra of Inorganic and Coordination Compounds, Part A: Theory and Applications in Inorganic Chemistry*; 5th Edition, Wiley Interscience: New York, 1997.
18 F. Xu, K. Matsumoto and R. Hagiwara, *Chem. Eur. J.*, 2010, **16**, 12970–12976.
19 R. D. Shannon, *Acta Crystallogr. Sect. A*, 1976, **32**, 751–767.
20 C. K. Lee, H. H. Peng and I. J. B. Lin, *Chem. Mater.*, 2004**, 16**, 530–536.
21 C. Hardacre, J. D. Holbrey, P. B. McCormac, S. E. J. McMath, M. Nieuwenhuyzen and K. R. Seddon, *J. Mater. Chem.*, 2001, **11**, 346–350.
22 K. M. Lee, C. K. Lee and I. J. B. Lin, *Chem. Commun.*, 1997, 899–900.

23 K. Matsumoto, R. Hagiwara, R. Yoshida, Y. Ito, Z. Mazej, P. Benkič, B. Žemva, O. Tamada, H. Yoshino and S. Matsubara, *J. Chem. Soc. Dalton Trans.*, 2004, 144–149.
24 K. Goossens, K. Lava, P. Nockemann, K. Van Hecke, L. Van Meervelt, P. Pattison, K. Binnemans and T. Cardinaels, *Langmuir*, 2009, **25**, 5881–5897.
25 I. Dierking, *Textures of Liquid Crystals*, WILEY-VCH, Weinhelm, 2003.
26 T. Kanatani, R. Ueno, K. Matsumoto, T. Nohira and R. Hagiwara, *J. Fluorine Chem.*, 2009, **130**, 979–984.

TOC Graphic and Summary for *Dalton Transactions*

Effects of Alkyl Chain Length and Anion Size on Thermal and Structural Properties for 1-Alkyl-3-methylimidazolium Hexafluorocomplex Salts (C_xMImAF_6, x = 14, 16, and 18; A = P, As, Sb, Nb, and Ta)

Fei Xu, Kazuhiko Matsumoto and Rika Hagiwara

Dalton Trans., XXXX, **XX**, XXXX-XXXX

A series of 1-alkyl-3-methylimidazolium hexafluorocomplex salts (C_xMImAF_6, x = 14, 16, and 18, A = P, As, Sb, Nb, and Ta) have been prepared and characterized by differential scanning calorimetry, polarized optical microscopy, and X-ray diffraction.